Computing the cut locus of a Riemannian manifold via optimal transport

Enrico Facca, Luca Berti, Francesco Fassò, Mario Putti

ESAIM: M2AN 56 (2022) 1939–1954
https://doi.org/10.1051/m2an/2022059

ESAIM: Mathematical Modelling and Numerical Analysis
www.esaim-m2an.org

COMPUTING THE CUT LOCUS OF A RIEMANNIAN MANIFOLD *VIA* OPTIMAL TRANSPORT

Enrico Facca[1,*], Luca Berti[2], Francesco Fassò[3] and Mario Putti[3]

Abstract. In this paper, we give a new characterization of the cut locus of a point on a compact Riemannian manifold as the zero set of the optimal transport density solution of the Monge–Kantorovich equations, a PDE formulation of the optimal transport problem with cost equal to the geodesic distance. Combining this result with an optimal transport numerical solver, based on the so-called dynamical Monge–Kantorovich approach, we propose a novel framework for the numerical approximation of the cut locus of a point in a manifold. We show the applicability of the proposed method on a few examples settled on 2d-surfaces embedded in $\mathbb{R}^3$, and discuss advantages and limitations.

Mathematics Subject Classification. 35J70, 49K20, 49M25, 49Q20, 58J05, 65K10, 65N30.

Received June 14, 2021. Accepted July 6, 2022.

1. Introduction

Given a compact Riemannian manifold (M, g) of dimension n and a point $p \in M$, the cut locus C_p of p is, roughly speaking, the set of points where more than one minimizing geodesic starting from p arrives. For example, the cut locus of a point in a 2-sphere embedded in $\mathbb{R}^3$ is its anti-podal point.

The cut locus is a fundamental object of Riemannian geometry, *e.g.*, it determines the topology of M since $M \setminus C_p$ is diffeomorphic to an n-disk [11]. Moreover, the cut locus is intimately related to the singular set of the distance function [35] and thus to the points where caustics form. However, the construction of the cut locus of a point on a manifold is rather difficult and cut locus shape is known only in very special cases, for example, for revolution surfaces [6]. For these reasons there is a strong interest in its numerical construction.

The numerical approximation of the cut locus of p has seen only sparse and diverse attempts in the past. For manifolds for which explicit parametrizations are available, the cut locus can be found by studying where geodesics collide [43] or studying conjugate points and Jacobi fields [7, 10] (we refer the reader to these two articles for the definition of such mathematical objects). However, when triangulated manifolds are considered, it is hard to extend these approaches. In [30] the exponential map is approximated by means of piecewise polynomial interpolation, and follow the geodesics starting from p until they are no longer minimal. Direct

Keywords and phrases. Cut locus, Riemannian geometry, Optimal Transport problem, Monge–Kantorovich equations, geodesic distance.

[1] Inria, Univ. Lille, CNRS, UMR 8524 – Laboratoire Paul Painlevé, 59000 Lille, France.

[2] Cemosis, IRMA UMR 7501, CNRS, Université de Strasbourg, Strasbourg, France.

[3] Department of Mathematics "Tullio Levi-Civita", University of Padua, Via Trieste 63, Padova, Italy.

*Corresponding author: enrico.facca@inria.fr

numerical evaluation of geodesics emanating from p is another approach often proposed. This is the method of choice in [36], who use a direct discretization by finite differences of the Riemannian partial differential equations. In [14] the authors construct the geodesics from the shortest paths in a graph constructed on the point data defining the manifold. All these methods require some sort of smoothing at cut points to cope with the ill-conditioning arising from the tracking of the distance along geodesics. As an alternative to geodesic-following methods, Crane *et al.* [12] approximate the geodesic distance by means of the numerical solution of the heat kernel defined on the manifold. The cut locus is then identified as the set of points where the trace of the Hessian of the distance explodes, thus again requiring some sort of smoothing for proper approximation. A similar strategy was adopted in [34].

To overcome these limitations, in [26] the authors propose a characterization of the cut locus as the limit in the Hausdorff sense of a variationally-defined thawed region around the cut locus. This allows the construction of a convergent finite-element-based numerical approximation of the cut locus which is described and analyzed in [27].

In this paper we propose a novel characterization of the cut locus based on Optimal Transport (OT) theory and exploit it to derive a stable and accurate numerical method for its approximation on compact Riemannian manifolds. The cut locus has been used extensively together with its properties in the analysis of the regularity of optimal transport problems [23–25, 48]. However, to the best of our knowledge, our characterization of the cut locus has never been proposed before.

In OT problems, one looks for the optimal strategy to re-allocate a non-negative measure f^+ into another non-negative measure f^- with equal mass, given a cost for transporting one unit of mass (see [2, 42, 46, 47] for a complete overview of the topic). When the transport takes place in a Riemannian manifold with the geodesic distance as cost, the solutions of the OT problem can be deduced from the solution of a nonlinear system of PDEs known as Monge–Kantorovich equations (MK equations). We denote the solution of the MK equations by (u^*, μ^*). The first element of the solution pair, the so-called *Kantorovich potential* u^*, is a continuous function with Lipschitz constant equal to 1. Moreover, its gradient is tangent to the paths (called rays) along which optimal transport movements occur, which are geodesics [39]. The second solution element, the so-called *Optimal Transport Density* (OTD) μ^*, is a non-negative measure on M that describes the mass flux through each portion of the manifold in an optimal transportation schedule from f^+ into f^-.

A fundamental property of μ^* is that it decays towards zero at the endpoints of the geodesics along which the mass is moved ([16], [9], Thm. 3). This fact suggests that if we take $f^+ = \mathrm{d}V_g(M)\delta_p$ and $f^- = \mathrm{d}V_g$ (where δ_p denotes the Dirac measure centered at p, $\mathrm{d}V_g$ is the volume form induced by the metric g, and $\mathrm{d}V_g(M)$ is the measure of M), the OTD restricted to all geodesics starting at point p tends to zero when approaching the points that form the cut locus of p in M. This intuition is confirmed by the following theorem, which represents our characterization of C_p:

Theorem 1.1. *Let (M, g) be a compact and geodesically complete Riemannian manifold of dimension n with no boundary. Given a point $p \in M$, the OTD μ^* solution of the MK equations with $f^+ = \mathrm{d}V_g(M)\delta_p$ and $f^- = \mathrm{d}V_g$ admits, in the set $M \setminus \{p\}$, a continuous density $\underline{\mu}$ with respect to the volume form $\mathrm{d}V_g$ whose zero set coincides with C_p i.e.,*

$$\mu^* = \underline{\mu}\,\mathrm{d}V_g,\ C_p = \big\{x \in M \setminus \{p\} : \underline{\mu}(x) = 0\big\}.$$

Based on this characterization, we propose a new variationally-based numerical scheme to approximate the cut locus on compact surfaces by means of the numerical solution of the MK equations. For the latter, we adopt the approach described in [4], where the discrete Dynamical Monge–Kantorovich (DMK) framework described in [18, 19] is extended to $\mathbb{R}^3$-embedded surfaces. We show the effectiveness of the proposed numerical approach by identifying the cut locus of the following triangulated surfaces: a torus, for which the cut locus is known, and two test cases borrowed from [30] to show the applicability to generic surfaces.

The paper is organized as follows. First we present all the Riemannian objects required for the definition of the cut-locus, together with some of its properties. Then, in Section 3 we recall the definition of the Optimal Transport Problem with cost equal to the geodesic distance, and the MK equations. Section 4 is dedicated to the

connection of the MK equations with the cut-locus, and ends with the proof of Theorem 1.1. Finally, Section 5 is dedicated to the presentation of the proposed numerical approach to identify the cut locus of triangulated surfaces *via* the DMK strategy and concludes with some numerical experiments.

2. The cut locus of a point on a Riemannian Manifold

We consider a geodesically complete and compact Riemannian manifold (M, g) with no boundary, equipped with a smooth metric g. We denote by $\langle v, w\rangle_{g(x)}$ the application of the metric g evaluated at x to the two vectors $v, w \in T_xM$. The symbols ∇_g, $|\cdot|_g$, and $\mathrm{d}V_g$ are used to identify the gradient operator, the vector norm, and the volume form induced by the metric tensor g on M. The distance between two points $x, y \in M$ is defined as:

$$\mathrm{dist}_g(x,y) = \inf_{\sigma}\left\{ \int_0^1 \sqrt{\langle \dot\sigma(s), \dot\sigma(s)\rangle_{g(\sigma(s))}}\,\mathrm{d}s \;:\; \begin{array}{c} \sigma \in \mathcal{C}^1([0,1], M) \\ \sigma(0) = x, \sigma(1) = y \end{array} \right\}.$$

Given a point $p \in M$, we denote with $\exp_p : T_pM \to M$ the exponential map of (M, g) at p and with $\exp_p^{-1}$ its inverse, where well defined.

2.1. Cut locus of a point

We now give the definition and some properties of the cut locus C_p of a point $p \in M$ and of all the related objects that will be used in the sequel (see [40]). Figure 1 illustrates graphically these definitions for a torus embedded in $\mathbb{R}^3$.

Definition 2.1. Let (M, g) be a compact and geodesically complete Riemannian manifold of dimension n, and consider a point $p \in M$. Let U_pM be the set of unit tangent vectors at p, *i.e.*:

$$U_pM := \Big\{ \theta \in T_pM : \langle \theta, \theta\rangle_{g(p)} = 1 \Big\}.$$

The *cut time* $\mathcal{T}_p(\theta)$ of $\theta \in U_pM$ is defined as:

$$\mathcal{T}_p(\theta) := \sup\big\{ t \geq 0 \;:\; \exp_p(s\theta)_{0\leq s<t} \text{ is a minimizing geodesic} \big\}. \tag{2.1}$$

The sets:

$$\hat I_p := \{ t\theta \;:\; \theta \in U_pM,\, 0 < t < \mathcal{T}_p(\theta)\} \subset T_pM \quad \text{and} \quad I_p := \exp_p\Big(\hat I_p\Big) \subset M \tag{2.2}$$

are called the *injectivity domain* and the *interior set* at p. Note that $\exp_p$ is a diffeomorphism from $\hat I_p$ to I_p, thus $\exp_p^{-1}$ is defined from I_p to $\hat I_p$.

The sets:

$$\hat C_p := \{ \mathcal{T}_p(\theta)\theta : \theta \in U_pM\} \subset T_pM \quad \text{and} \quad C_p := \exp_p\Big(\hat C_p\Big) \subset M$$

are called, respectively, the *tangent cut locus* and the *cut locus* of p.

Lemma 2.2 (Properties of the cut time [31])**.** *The functions $\mathcal{T}_p$ and $\mathcal{T}_p^{\mathcal{B}}$ defined in equations (2.1) and (2.4) are Lipschitz continuous.*

Lemma 2.3 (Properties of the cut locus [40])**.** *The manifold M is the union of three disjoint sets: the point p, the interior set I_p, and the cut locus C_p. Moreover, C_p is a null set of the volume form $\mathrm{d}V_g$.*

Lemma 2.4 (Properties of the injectivity domain [40])**.** *The injectivity domain $\hat I_p$ is a star shaped subset of T_pM with boundary given by $\hat C_p$.*

As an example, Figure 1 shows the cut locus C_p (red color) of a point p lying on the external "equator" of the torus (from [28, 33]) and an approximation of the tangent cut locus $\hat C_p \subset T_pM$ (blue color) obtained by solving numerically the equations of the geodesic curves emanating from $p = (3, 0, 0)$.

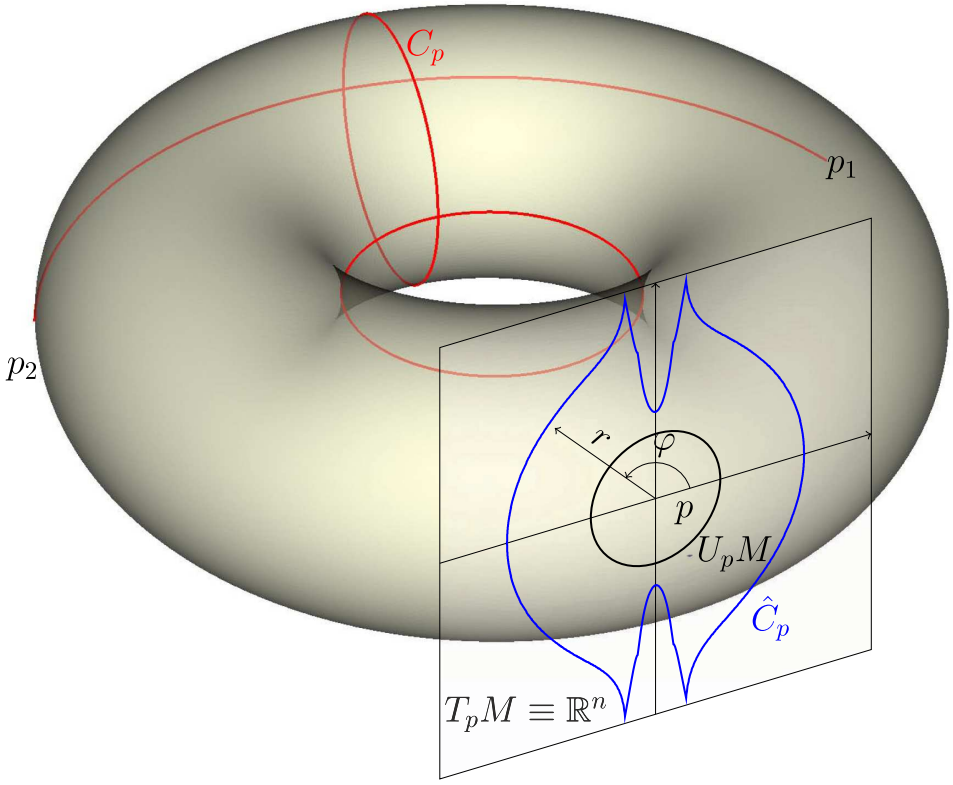

FIGURE 1. The tangent cut locus and the cut locus of a point on the torus with major and minor radi $r_{\max} = 2$ and $r_{\min} = 1$ embedded in $\mathbb{R}^3$. The red curves identify the cut locus of the point $p = (R, 0, 0)$ with $R := r_{\max} + r_{\min}$ located on the external "equator". Note that the cut locus is formed by the internal "equator", the opposite "meridian", and a portion of the external "equator" connecting the two points $p_1 = (R\cos(\alpha), R\sin(\alpha), 0)$ and $p_2 = (R\cos(\alpha), -R\sin(\alpha), 0)$ with $\alpha = \pi r_{\min}/\sqrt{R r_{\min}}$ (formulae taken from [33], Thm. 9). The blue lines represent a scaled approximation of the tangent cut locus $\hat{C}_p$ obtained by straight-forward numerical approximation of the geodesics emanating from p.

2.2. Riemannian polar coordinates

Next we give workable expressions, in local coordinates, for these cut locus-related quantities. To this aim, we need to fix proper charts and local coordinates. In view of Lemma 2.4, it is convenient to use Riemannian polar coordinates (see [32]). However we need to be slightly pedantic here about their definition and properties because we will need to show that our solution of the OT problem is free of the singularities introduced by such coordinate systems.

Any set of these coordinates depends on the choice of a $g(p)$-orthonormal basis $\mathcal{B} = \{e_1^{\mathcal{B}}, \dots, e_n^{\mathcal{B}}\}$ of T_pM, which allows the identification of T_pM with $\mathbb{R}^n$ *via* the map $v \mapsto (v_1^{\mathcal{B}}, \dots, v_n^{\mathcal{B}})$ with $v_i^{\mathcal{B}} := \langle v, e_i^{\mathcal{B}} \rangle_{g(p)}$ for $i = 1, \dots, n$. We define the map

$$\Psi^{\mathcal{B}} : \hat{I}_p \to \mathbb{R}_+ \times \mathcal{S}^{n-1}, \ v \mapsto \left(|v|_g, \frac{v^{\mathcal{B}}}{|v|_g} \right)$$

and, denoting by $\mathcal{S}^{n-1}_\circ = \mathcal{S}^{n-1} \setminus (0, \dots, \pm 1)$, we introduce the (Euclidean) polar coordinates

$$P : \mathbb{R}_+ \times \mathcal{S}^{n-1}_\circ \to \mathbb{R}_+ \times \mathbb{U}^{n-1}, \quad \mathbb{U}^{n-1} =]0, \pi[^{n-2} \times \mathcal{S}^1$$
$$(r, y) \mapsto (r, \varphi_1(y), \dots, \varphi_{n-1}(y))$$

where $\varphi = (\varphi_1, \dots, \varphi_{n-1})$ are the $n-1$ spherical coordinates parametrizing $\mathcal{S}^{n-1}$ (see [5] for explicit formulas). Then, the Riemannian polar coordinates relative to the basis $\mathcal{B}$ is the map $\phi_p^{\mathcal{B}} = P \circ \Psi^{\mathcal{B}} \circ \exp_p^{-1}$. Explicitly, this is given by:

$$\begin{aligned} \phi_p^{\mathcal{B}} : I_p^{\mathcal{B}} \overset{\exp_p^{-1}}{\longrightarrow} \hat{I}_p^{\mathcal{B}} \overset{\Psi^{\mathcal{B}}}{\longrightarrow} \mathbb{R}_+ \times \mathcal{S}^{n-1}_\circ \overset{P}{\longrightarrow} \mathbb{R}_+ \times \mathbb{U}^{n-1} \\ x \longmapsto v := \exp_p^{-1}(x) \longmapsto \left(|v|_g, \frac{v^{\mathcal{B}}}{|v|_g} \right) \longmapsto \left(|v|_g, \varphi\left(\frac{v^{\mathcal{B}}}{|v|_g} \right) \right) \end{aligned} \tag{2.3}$$

where the sets $I_p^{\mathcal{B}} \subset I_p$ and $\hat{I}_p^{\mathcal{B}} \subset \hat{I}_p$ are the preimages under the maps $\Psi^{\mathcal{B}} \circ \exp_p^{-1}$ and $\Psi^{\mathcal{B}}$ of $\mathbb{R}_+ \times \mathcal{S}^{n-1}_\circ$, respectively. Note that $|v|_g = \mathrm{dist}_g(p, x)$.

Remark 2.5. The set $I_p^{\mathcal{B}}$ coincides with I_p minus a geodesic curve that passes through p and depends on the basis $\mathcal{B}$.

It is clear that, given $\mathcal{B}$, there exists a one-to-one correspondence between elements of $U_pM \setminus \{e_n^{\mathcal{B}}, -e_n^{\mathcal{B}}\}$ and $\mathbb{U}^{n-1}$. Thus, we define the cut time function $\mathcal{T}_p^{\mathcal{B}}$ that maps the angle variables φ into the cut time of the corresponding unit vector in the tangent space *i.e.*,

$$\mathcal{T}_p^{\mathcal{B}} : \mathbb{U}^{n-1} \to \mathbb{R}_+, \ \mathcal{T}_p^{\mathcal{B}}(\varphi) := \mathcal{T}_p \circ \left(\Psi^{\mathcal{B}}\right)^{-1} \circ P^{-1}(1, \varphi) \quad \forall \varphi \in \mathbb{U}^{n-1}. \tag{2.4}$$

Lemma 2.6 (Properties of polar coordinates [32])**.** *For any $g(p)$-orthonormal basis $\mathcal{B}$, the matrix representing the metric $g|_{I_p^{\mathcal{B}}}$ written in Riemannian polar coordinates has the block-diagonal expression*

$$g^{\mathcal{B}}(r, \varphi) = \begin{pmatrix} 1 & 0 \\ 0 & h^{\mathcal{B}}(r, \varphi) \end{pmatrix},$$

where $h^{\mathcal{B}}(r, \varphi)$ is a $(n-1) \times (n-1)$ symmetric and positive-definite matrix.

We denote

$$\mathcal{J}^{\mathcal{B}}(r, \varphi)\, \mathrm{d}r \wedge \mathrm{d}\varphi_1 \wedge \ldots \wedge \mathrm{d}\varphi_{n-1}$$

the volume form $\mathrm{d}V_g$ expressed in polar coordinates in the interior set I_p.

Lemma 2.7. *The function $\mathcal{J}^{\mathcal{B}}$ factorizes as follows:*

$$\mathcal{J}^{\mathcal{B}}(r, \varphi) = G^{\mathcal{B}}(r, \varphi) J(r, \varphi), \tag{2.5}$$

where $G^{\mathcal{B}} : \mathbb{R}_+ \times \mathbb{U}^{n-1} \to \mathbb{R}_+$ is given by

$$G^{\mathcal{B}}(r, \varphi) = \sqrt{\det\left(g \circ \left(\phi_p^{\mathcal{B}}\right)^{-1}(r, \varphi) \right)}, \tag{2.6}$$

and J is the absolute value of the determinant of the Jacobian matrix of P^{-1} and is given by:

$$J(r, \varphi_1, \varphi_2, \dots, \varphi_{n-2}) = r^{n-1} \sin^{n-2}(\varphi_1) \sin^{n-3}(\varphi_2) \dots \sin(\varphi_{n-2}). \tag{2.7}$$

Proof. The proof comes directly from the appropriate composition of the relevant functions defined above. □

Let $SO(n, T_pM)$ be the set of all proper ($\det = +1$) linear $g(p)$-isometries of T_pM. Given a $g(p)$-orthonormal basis $\mathcal{B} = \{e_1^{\mathcal{B}}, \dots, e_n^{\mathcal{B}}\}$ of T_pM, we associate to any $\hat{R} \in SO(n, T_pM)$ the matrix $R^{\mathcal{B}} \in SO(n)$ with entries $R^{\mathcal{B}}_{i,j} = \left\langle e_i^{\mathcal{B}}, \hat{R} e_j^{\mathcal{B}} \right\rangle_{g(p)}$. Also, we denote by $\hat{R}\mathcal{B}$ the rotated basis $\left\{\hat{R}e_1^{\mathcal{B}}, \dots, \hat{R}e_n^{\mathcal{B}}\right\}$.

Lemma 2.8. *For any $g(p)$-orthonormal basis $\mathcal{B}$ and any $\hat{R} \in SO(n, T_pM)$,*

$$G^{\hat{R}\mathcal{B}} \circ P\big(r, R^{\mathcal{B}} y\big) = G^{\mathcal{B}} \circ P(r, y)$$

for all $r \in \mathbb{R}_+$ and $y \in \mathcal{S}_\circ^{n-1}$ such that $\left(\hat{R}\right)^T y \in \mathcal{S}_\circ^{n-1}$.

Proof. This follows from the fact that, as we verify,

$$\left(\Psi^{\hat{R}\mathcal{B}}\right)^{-1}(r, R^{\mathcal{B}} y) = \left(\Psi^{\mathcal{B}}\right)^{-1}(r, y), \tag{2.8}$$

for all r, y as in the statement. From now on, we write for short R for $R^{\mathcal{B}}$. First note that, $\forall v \in T_pM$, $v^{\hat{R}\mathcal{B}} = R^T v^{\mathcal{B}}$ and $\left(\hat{R}v\right)^{\mathcal{B}} = Rv^{\mathcal{B}}$. Thus

$$\begin{aligned}\Psi^{\hat{R}\mathcal{B}}\left(\hat{R}v\right) &= \left(\left|\hat{R}v\right|_g, \frac{\left(\hat{R}v\right)^{\hat{R}\mathcal{B}}}{\left|\hat{R}v\right|_g}\right) = \left(|v|_g, \frac{R^T\left(\hat{R}v\right)^{\mathcal{B}}}{|v|_g}\right) \\ &= \left(|v|_g, \frac{R^T R v^{\mathcal{B}}}{|v|_g}\right) = \Psi^{\mathcal{B}}(v).\end{aligned}$$

This implies that, if $(r, y) = \Psi^{\mathcal{B}}(v)$ then

$$\begin{aligned}\Psi^{\hat{R}\mathcal{B}} \circ \left(\Psi^{\mathcal{B}}\right)^{-1}(r, y) = \Psi^{\hat{R}\mathcal{B}}(v) &= \left(|v|_g, \frac{v^{\hat{R}\mathcal{B}}}{|v|_g}\right) \\ &= \left(|v|_g, \frac{Rv^{\mathcal{B}}}{|v|_g}\right) = (r, Ry),\end{aligned}$$

namely equation (2.8). □

3. Monge–Kantorovich equations on manifolds

In this section we present the Monge–Kantorovich equations (MK equations), an equivalent PDE formulation of the optimal transport problem on a Riemannian manifold with geodesic distance as transport cost. We use the formulation described in [8, 39], assuming that one of the transported measures f^+ and f^- on M admits a density with respect to the volume form $\mathrm{d}V_g$. Under these assumptions the MK equations can be written as the problem of finding a pair (u^*, μ^*), where u^* is a continuous function with Lipschitz constant equal to 1 and μ^* is a non-negative measure, that solves

$$-\mathrm{div}_g(\mu^* \nabla_g u^*) = f^+ - f^- \quad \text{on } M, \tag{3.1a}$$

$$|\nabla_g u^*|_g \le 1 \quad \text{on } M, \tag{3.1b}$$

$$|\nabla_g u^*|_g = 1 \quad \mu^* - a.e., \tag{3.1c}$$

where equation (3.1a) must be interpreted in the following weak form:

$$\int_M \langle \nabla_g u^*, \nabla_g \phi \rangle_g \, \mathrm{d}\mu^* = \int_M \phi \, \mathrm{d}f^+ - \int_M \phi \, \mathrm{d}f^-, \ \forall \phi \in \mathcal{C}^1(M). \tag{3.2}$$

The components of the solution pair (u^*, μ^*) of the above system are named Kantorovich potential and OTD, respectively.

The following lemma summarizes a series of results on the solution of the MK equations from [2, 13, 16, 21, 22, 39, 41].

Lemma 3.1 (Properties of Monge–Kantorovich equations)**.** *The Kantorovich potential u^* is unique up to a constant within the support of μ^* (outside supp(μ^*) there exist infinitely many functions u that satisfy Eq. (3.1)).*

If either f^+ or f^- (or both) is absolutely continuous with respect to the volume form $\mathrm{d}V_g$, then the OTD μ^* is unique and is absolutely continuous with respect to $\mathrm{d}V_g$.

Remark 3.2. Without *a priori* knowledge of the integrability of μ^*, guaranteed by Lemma 3.1 in our problem, the formulation of the MK equations requires the notion of gradient with respect to a measure [8].

Intuitively speaking, the link between OT and the solution (u^*, μ^*) of the MK equations equation (3.1) is as follows. The OTD μ^* can be seen as a measure of the flux through each portion of the manifold in the optimal reallocation of f^+ into f^-. Mass moves along disjoint transport rays that follow the direction of the gradient of the Kantorovich potential u^*. Intuitively, these transport rays are geodesics connecting points in the support of f^+ with points in the support of f^- (we refer the reader to [2] for the proper definition of transport rays). Under certain properties of the transported measures f^+ and f^- (L^∞ densities and disjoint supports), Evans and Gangbo [16] proved that the OTD tends to zero at the endpoints of each transport ray.

4. OT characterization of C_p

From the property of the decay of the OTD along the transport rays we devise the following strategy for the search of the cut locus: we set $f^+ = \mathrm{d}V_g(M)\delta_p$ (with δ_p the Dirac delta centered at p) and $f^- = \mathrm{d}V_g$ and look at the zero-set of μ^*. The intuition is that in the optimal reallocation of the Dirac mass centered at p, the mass is "sent" from p to all the points of M along geodesics. The mass is progressively "absorbed" by the constant sink term $f^- = \mathrm{d}V_g$ until we reach those points where mass is coming also from a different direction. At those points, μ^* becomes zero. For a cleaner understanding of this idea and of the properties of the OTD, we present a simple example on the unit circle $\mathcal{S}^1$.

Example 4.1. On the unit circle $\mathcal{S}^1 = \{x^2 + y^2 = 1\}$ we consider the point $p = (1, 0)$ and source terms given by $f^+ = 2\pi\delta_p$ and $f^- = 1\,\mathrm{d}\varphi$. Using the angle coordinate $\varphi \in \mathcal{S}^1$ the Kantorovich potential and the OTD are given by:

$$u^*(\varphi) = -|\varphi|, \ \mu^*(\varphi) = \pi - |\varphi|, \ \varphi \in \mathcal{S}^1. \tag{4.1}$$

The graphs of μ^* and the transported measures are reported in Figure 2. The OTD μ^* progressively decays moving away from the point p, until the antipodal point is reached, where it vanishes. According to the definition given in [2], in this example the arcs $]-\pi, 0[$ and $]0, \pi[$ are the transport rays.

The extension of this idea to a general manifold leads to the following theorem, which is a more complete version of Theorem 1.1.

Theorem 4.2. *Let (M, g) be a compact and geodesically complete Riemannian manifold of dimension n and with no boundary. Consider a point $p \in M$ and the measures*

$$f^+ = \mathrm{d}V_g(M)\delta_p, \ f^- = \mathrm{d}V_g. \tag{4.2}$$

Let (u^*, μ^*) be the solution of the MK equations with measures given by equation (4.2). Then:

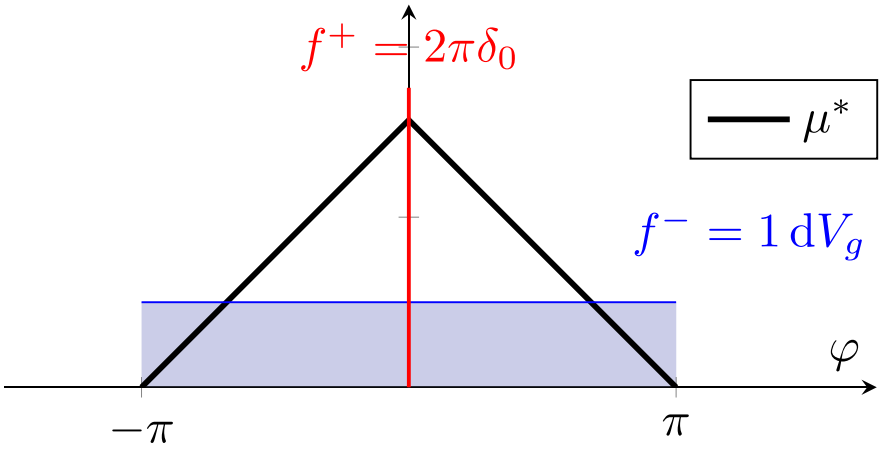

FIGURE 2. Graph of the OTD μ^* (black) solution of the MK equations in the unit circle $\mathcal{S}^1$ (the point $-\pi$ is identified with π) with $f^+ = 2\pi\delta_0$ (red) and $f^- = \mathrm{d}\varphi$ (blue).

(i) *the Kantorovich Potential u^* coincides with minus the geodesic distance from p:*

$$u^*(x) = -\operatorname{dist}_g(x,p); \tag{4.3}$$

(ii) *when restricted to $M \setminus \{p\}$, the OTD μ^* admits a* continuous *density $\underline{\mu}$ with respect to the volume form $\mathrm{d}V_g$:*

$$\mu^* = \underline{\mu}\,\mathrm{d}V_g,\ \ \underline{\mu} \in \mathcal{C}^0(M \setminus \{p\});$$

(iii) *the zero set of $\underline{\mu}$ coincides with the cut locus C_p of p:*

$$C_p = \big\{x \in M \setminus \{p\} : \underline{\mu}(x) = 0\big\};$$

(iv) *for any $g(p)$-orthonormal basis $\mathcal{B}$, the local representative $\underline{\mu}^{\mathcal{B}} := \underline{\mu} \circ (\phi_p^{\mathcal{B}})^{-1}$ in the chart $\phi_p^{\mathcal{B}}$ of the function $\underline{\mu}$ is given by*

$$\underline{\mu}^{\mathcal{B}}(r,\varphi) = \frac{1}{G^{\mathcal{B}}(r,\varphi) r^{n-1}} \int_r^{\mathcal{T}_p^{\mathcal{B}}(\varphi)} G^{\mathcal{B}}(s,\varphi) s^{n-1}\,\mathrm{d}s, \tag{4.4}$$

for all $(r,\varphi) \in \phi_p^{\mathcal{B}}\big(I_p^{\mathcal{B}}\big) \subset \mathbb{R}_+ \times \mathbb{U}^{n-1}$.

Proof. We first observe that thanks to Lemma 2.8, given two $g(p)$-orthonormal basis $\mathcal{B}$ and $\mathcal{B}'$ the functions $\underline{\mu}^{\mathcal{B}} \circ \phi_p^{\mathcal{B}}$ and $\underline{\mu}^{\mathcal{B}'} \circ \phi_p^{\mathcal{B}'}$ coincide in the intersection of their domains. Therefore, there exists a *continuous* function $\underline{\mu}$ on I_p with local representative $\underline{\mu}^{\mathcal{B}}$ in any chart $\phi_p^{\mathcal{B}}$ given by equation (4.4). Moreover, since for every $\mathcal{B}$ $\underline{\mu}^{\mathcal{B}}$ is positive in its domain $\phi_p^{\mathcal{B}}(I_p^{\mathcal{B}})$ and, for every φ,

$$\lim_{r \to \mathcal{T}_p^{\mathcal{B}}(\varphi)} \underline{\mu}^{\mathcal{B}}(r,\varphi) = 0,$$

the function $\underline{\mu}$ admits a (unique) continuous extension on $I_p \cup C_p = M \setminus \{p\}$, which we will continue to denote with $\underline{\mu}$. This extension is non-negative and its zero set coincides with the cut locus of p. This proves statement (iii). The term $G^{\mathcal{B}}$, defined in equation (2.6), is clearly bounded from above and from below. Hence, the integral in equation (4.4) tends to zero as $r \to \mathcal{T}_p^{\mathcal{B}}(\varphi)$.

Now, we note that the source term f^- in equation (4.2) is absolutely continuous with respect to the volume form $\mathrm{d}V_g$. Thus, Lemma 3.1 ensures that the OTD μ^* admits a unique density with respect to the volume form $\mathrm{d}V_g$. We now show that, with $\underline{\mu}$ defined above, the pair (u^*, μ^*) given by

$$u^*(x) = -\operatorname{dist}_g(x,p),\ \ \mu^* \overset{a.e.}{=} \underline{\mu}\,\mathrm{d}V_g, \tag{4.5}$$

solves equation (3.1). It is clear that u^* satisfies the constraints in equations (3.1c) and (3.1b). Thus, we only have to prove that (u^*, μ^*) solves equation (3.2) for f^+ and f^- in equation (4.2) *i.e.*,

$$\int_M \langle \nabla_g u^*, \nabla_g \phi \rangle_g \,\mathrm{d}\mu^* = \int_M (\,\mathrm{d}V_g(M))\phi\delta_p - \int_M \phi\,\mathrm{d}V_g \qquad \forall \phi \in \mathcal{C}^1(M). \tag{4.6}$$

For all $\phi \in \mathcal{C}^1(M)$, the right-hand side RHS of the above equation can be evaluated as

$$\mathrm{RHS} = (\,\mathrm{d}V_g(M))\phi(p) - \int_M \phi\,\mathrm{d}V_g. \tag{4.7}$$

We know, from Lemma 2.3 and Remark 2.5, that for any $g(p)$-orthonormal basis $\mathcal{B}$ the set $M\backslash I_p^{\mathcal{B}}$ has zero measure on M. Thus, we can restrict the integrals on the left-hand side of equation (4.6) to $I_p^{\mathcal{B}}$ and use the Riemannian polar coordinates to compute them. Write $\phi^{\mathcal{B}} = \phi \circ (\phi_p^{\mathcal{B}})^{-1}$ and $u^{\mathcal{B}} = u^* \circ (\phi_p^{\mathcal{B}})^{-1}$. Thus, $u^{\mathcal{B}}(r,\varphi) = -r$ and the left-hand side LHS of equation (4.6) becomes:

$$\mathrm{LHS} = \int_{\mathbb{U}^{n-1}} \int_0^{\mathcal{T}_p^{\mathcal{B}}(\varphi)} \nabla u^{\mathcal{B}}(r,\varphi) \cdot g^{\mathcal{B}}(r,\varphi)^{-1} \nabla \phi^{\mathcal{B}}(r,\varphi) \underline{\mu}^{\mathcal{B}}(r,\varphi) \mathcal{J}^{\mathcal{B}}(r,\varphi)\,\mathrm{d}r\,\mathrm{d}\varphi.$$

Now, $\nabla u^{\mathcal{B}}(r,\varphi) = (-1, 0, \ldots, 0)$ and from Lemma 2.6 we have

$$\nabla u^{\mathcal{B}}(r,\varphi) \cdot g^{\mathcal{B}}(r,\varphi)^{-1} \nabla \phi^{\mathcal{B}}(r,\varphi) = -\partial_r \phi^{\mathcal{B}}(r,\varphi).$$

Thus, recalling equations (4.4) and (2.5) of Lemma 2.7

$$\mathrm{LHS} = -\int_{\mathbb{U}^{n-1}} \int_0^{\mathcal{T}_p^{\mathcal{B}}(\varphi)} \left(\int_r^{\mathcal{T}_p^{\mathcal{B}}(\varphi)} \mathcal{J}^{\mathcal{B}}(s,\varphi)\,\mathrm{d}s \right) \partial_r \phi^{\mathcal{B}}(r,\varphi)\,\mathrm{d}r\,\mathrm{d}\varphi.$$

Integration by parts yields:

$$\begin{aligned}\mathrm{LHS} = &-\int_{\mathbb{U}^{n-1}} \left(\left[\left(\int_r^{\mathcal{T}_p^{\mathcal{B}}(\varphi)} \mathcal{J}^{\mathcal{B}}(s,\varphi)\,\mathrm{d}s \right) \phi^{\mathcal{B}}(r,\varphi) \right]_0^{\mathcal{T}_p^{\mathcal{B}}(\varphi)} \right) \mathrm{d}\varphi \\ &+ \int_{\mathbb{U}^{n-1}} \left(\int_0^{\mathcal{T}_p^{\mathcal{B}}(\varphi)} \partial_r \left(\int_r^{\mathcal{T}_p^{\mathcal{B}}(\varphi)} \mathcal{J}^{\mathcal{B}}(s,\varphi)\,\mathrm{d}s \right) \phi^{\mathcal{B}}(r,\varphi)\,\mathrm{d}r \right) \mathrm{d}\varphi.\end{aligned}$$

The first term is evaluated by taking the separate limits as $r \to \mathcal{T}_p^{\mathcal{B}}(\varphi)$ and as $r \to 0$, with the former yielding zero. In conclusion,

$$\begin{aligned}\mathrm{LHS} &= \phi(p) \int_{\mathbb{U}^{n-1}} \int_0^{\mathcal{T}_p^{\mathcal{B}}(\varphi)} \mathcal{J}^{\mathcal{B}}(s,\varphi)\,\mathrm{d}s\,\mathrm{d}\varphi - \int_{\mathbb{U}^{n-1}} \int_0^{\mathcal{T}_p^{\mathcal{B}}(\varphi)} \mathcal{J}^{\mathcal{B}}(r,\varphi)\phi^{\mathcal{B}}(r,\varphi)\,\mathrm{d}r\,\mathrm{d}\varphi \\ &= (\,\mathrm{d}V_g(M))\phi(p) - \int_{I_p^{\mathcal{B}}} \phi\,\mathrm{d}V_g,\end{aligned}$$

and then LHS = RHS for all $\phi \in \mathcal{C}^1(M)$, proving equation (4.6). This shows that the pair (u^*, μ^*) in equation (4.5) solves of the MK equations for f^+ and f^- in equation (4.2). This proves statements (i), (ii), and (iv). Statement (iii) has already been proved. □

Remark 4.3. It is worth noting that, thanks to Theorem 4.2 and to the results in [19, 20], we can give a variational characterization of the OTD as the minimizer of:

$$\min_{\mu}\{\mathcal{L}_g(\mu) : \mu \in \mathcal{C}^0(M \setminus \{p\}, \mathbb{R}_+)\},$$

with $\mathcal{L}_g = \mathcal{E}_g + M_g$ and

$$\mathcal{E}_g(\mu) := \sup_{\phi \in \mathrm{Lip}\,(M)} \left\{ \int_M (\,\mathrm{d}V_g(M)\delta_p - \,\mathrm{d}V_g)\phi - \mu \frac{|\nabla_g \phi|^2}{2}\,\mathrm{d}V_g \right\},$$
$$\mathcal{M}_g(\mu) := \frac{1}{2}\int_M \mu\,\mathrm{d}V_g.$$

This provides a variational characterization of the cut locus of a point $p \in M$ as the zero set of the minimizer μ^* of $\mathcal{L}_g(\mu)$.

5. Numerical approximation of the cut locus

In this section we present our strategy for the calculation of the cut locus based on Theorem 4.2. Unfortunately, it is numerically challenging to look directly at the zero set of the expression for OTD μ^* given in equation (4.4). Indeed, this would require the approximation of the distance and cut time functions, *i.e.*, the same unknowns in the identification problem of the cut locus. As an alternative, at least in the case of a surface Γ embedded in $\mathbb{R}^3$, we approach the numerical solution of the MK equations equation (3.1) by means of the "dynamic" reformulation of the MK equations, called DMK, recently proposed in [18], analized in [20], and its finite-element-based discretization, described in [19]. More precisely, we use the extension to the surface setting of the DMK approach as described in [4], in which the numerical schemes developed in [19] are extended to the surface setting using the Surface Finite Element Method (SFEM) framework reviewed in [15].

We summarize here the fundamental steps of SFEM-DMK that impact on our goal of calculating the cut locus. First, let the surface Γ be decomposed with a geodesic triangulation $\Gamma = \mathcal{T}(\Gamma)$, formed by triangles whose edges are the geodesics between the vertices. Next, this triangulation is approximated by its piecewise linear interpolant $\Gamma_h = \mathcal{T}_h(\Gamma) = \cup\mathbb{E}_r$, *i.e.*, the union of 2-simplices $\mathbb{E}_r$ in $\mathbb{R}^3$ having the same vertices as $\mathcal{T}(\Gamma)$ (for more details see [15, 37]). Using Γ_h it is possible to define appropriate discrete geometric quantities, such as surface gradients and discrete finite element function spaces, that allow the numerical discretization of the MK equations on surfaces embedded in $\mathbb{R}^3$. We refer to [15] for details on SFEM and to [4] for details and application examples of SFEM to the DMK on surfaces.

In practice, the calculation of the cut locus takes place on the piecewise linear interpolation Γ_h of Γ by means of the SFEM discretization of the MK equations with $f^+ = \mathrm{d}V_g(\Gamma_h)\delta_p$ and $f^- = \mathrm{d}V_g$. To maintain stability we follow the procedure described in [19] whereby the Kantorovich potential u^* is interpolated on a uniformly refined mesh $\mathcal{T}_{h/2}(\Gamma_h) \subset \mathcal{T}_h(\Gamma_h)$ by piecewise linear polynomials, while the OT density μ^* is approximated on $\mathcal{T}_h(\Gamma_h)$ by piecewise constants. As a consequence, the approximated cut locus is formed by the union of the triangles $\mathbb{E}_r \in \mathcal{T}_h(\Gamma_h)$ where our numerically evaluated OTD, μ_h^*, is close to zero. Thus, we give the following definition of the approximate cut locus ($C_{p,h,\epsilon}$):

$$C_{p,h,\epsilon} := \{\cup\mathbb{E}_r \in \mathcal{T}_h(\Gamma_h) \text{ s.t. } (\mu_h^*)|_{\mathbb{E}_r} \leq \epsilon\}$$

where ϵ is an appropriate preselected tolerance.

Remark 5.1. The definition of this tolerance is crucial for a proper approximation of C_p. Indeed, it is rather difficult to approximate a one-dimensional structure, and more so single points, as a union of triangles of $\mathcal{T}_h(\Gamma)$, and we will see by experimentation that different values of ϵ lead to different $C_{p,h,\epsilon}$. Another difficulty arises from the use of the singular source term $f^+ = \mathrm{d}V_g(\Gamma)\delta_p$, which does not belong to the dual of $H^1(\Gamma)$. This is

a typical problem in applications and yields suboptimal SFEM convergence rates for u^*. To address this issue one may either use regularization along the lines of [44,45] or *a posteriori* error estimations to adapt the surface mesh. We choose not to employ any of these approaches since first order global accuracy is in any case enforced by the piecewise constant discretization of μ^*.

We would like to note that according to [1] the cut locus is stable under $\mathcal{C}^2$ perturbations of the domain or of the metric but stability may be lost in case of $\mathcal{C}^1$ perturbations. However, the ensuing experimental results show that our piecewise constant approximation of the transport density introduces enough regularization to our numerical solution, at least for the sample problems addressed in this work.

5.1. Numerical experiments

First we would like to note that a Python notebook reproducing the experiments presented in this section can be found at this link https://doi.org/10.5281/zenodo.5710660. The source code is available at the following repository https://gitlab.com/enrico_facca/dmk_solver (subdirectory FaccaBertiFassoPutti2021_CutLocus).

The first test case, described in Section 2.1 and shown in Figure 1, deals with the calculation of the cut locus C_p of a torus T with radii $r_{\max} = 2$ and $r_{\min} = 1$ with respect to the point $p = (3, 0, 0)$. The results of our simulations are shown in Figure 3. The top panels of the figure depict the $C_{p,h,\epsilon}$ obtained using a tolerance $\epsilon = 10^{-3}$ on four mesh refinement levels. It is clear that $C_{p,h,\epsilon}$ approximates the real cut locus with satisfactory accuracy already on the coarsest grid, with progressively improving resolution as expected by the higher refinement levels. The effect of the mesh finite size is clearly discernible but no instabilities in the identification of the cut locus are visible. Note that perturbations of Γ and g in the refinement step from $\mathcal{T}_h(\Gamma)$ to $\mathcal{T}_{h/2}(\Gamma)$ are not strictly $\mathcal{C}^{1,1}$-regular. However, we can view $\mathcal{T}_h(\Gamma)$ as a linear interpolation of Γ whose error can be bounded by h^2 times the norm of the second fundamental form of Γ [3,15,37]. This regularity is sufficient to provide empirical justification of the stability of our calculations. This rationale is further strengthened by the results at the finest grid level.

The $C_{p,h,\epsilon}$ for $\epsilon = 10^{-4}$ is shown in the bottom panel of Figure 3. A much better approximation of the real cut locus is displayed with increased level of details. However, one portion of the "internal equator" opposite to p is not identified. We can give a heuristic explanation for this phenomenon by looking at the explicit formula of the OTD in equation (4.4). Roughly, this formula predicts an increased value of the OTD in the regions of larger mass fluxes. In our case this corresponds to the region surrounding the internal equator, where the geodesics starting at p arrive with a small angle with respect to the internal great circle. Thus, the values of μ_h^* in these triangles are relatively large, and the approximation of the cut locus becomes problematic when using an absolute identification criterion. This problem could of course be relieved by employing standard strategies that combine relative error measures and adaptive mesh refinements, tasks that go beyond the purpose of this paper.

The second test case is taken from Section 5 of [30] where the authors consider the triaxial ellipsoid given by

$$E := \{(x, y, z) \in \mathbb{R}^3 : (x/0.2)^2 + (y/0.6)^2 + z^2 = 1\}.$$

The cut loci of two points in E are studied. The first point considered is $p^1 = (-0.115470, 0, 0.816497)$, an umbilic point whose cut locus consists of a single point. The second point is $p^2 = (-0.151128, -0.350718, 0.295520)$ and its cut locus is an arc on the opposite side of the ellipsoid [29].

In Figure 4 we report the spatial distribution of the approximate OTD μ_h^* associated to the points p^1 and p^2, on the top and bottom panels, respectively. We start from an initial triangulation $\mathcal{T}_h$ of the ellipsoid with 534 nodes and 1064 triangles, obtained by means of the software described in [38]. We generate a sequence of finer grids conformally refining $\mathcal{T}_h$ and "lifting" the added nodes (the mid-points of the edges of the triangles) to the ellipsoid. We report the spatial distribution of μ_h^* only on those triangles where $\mu_h^* < 0.04$ to appreciate the decay of the OTD as it approaches the cut locus. Already at the coarsest grid, the region were μ_h^* attains the lowest values (in black in Fig. 4) strongly resembles the approximate cut locus computed in [30].

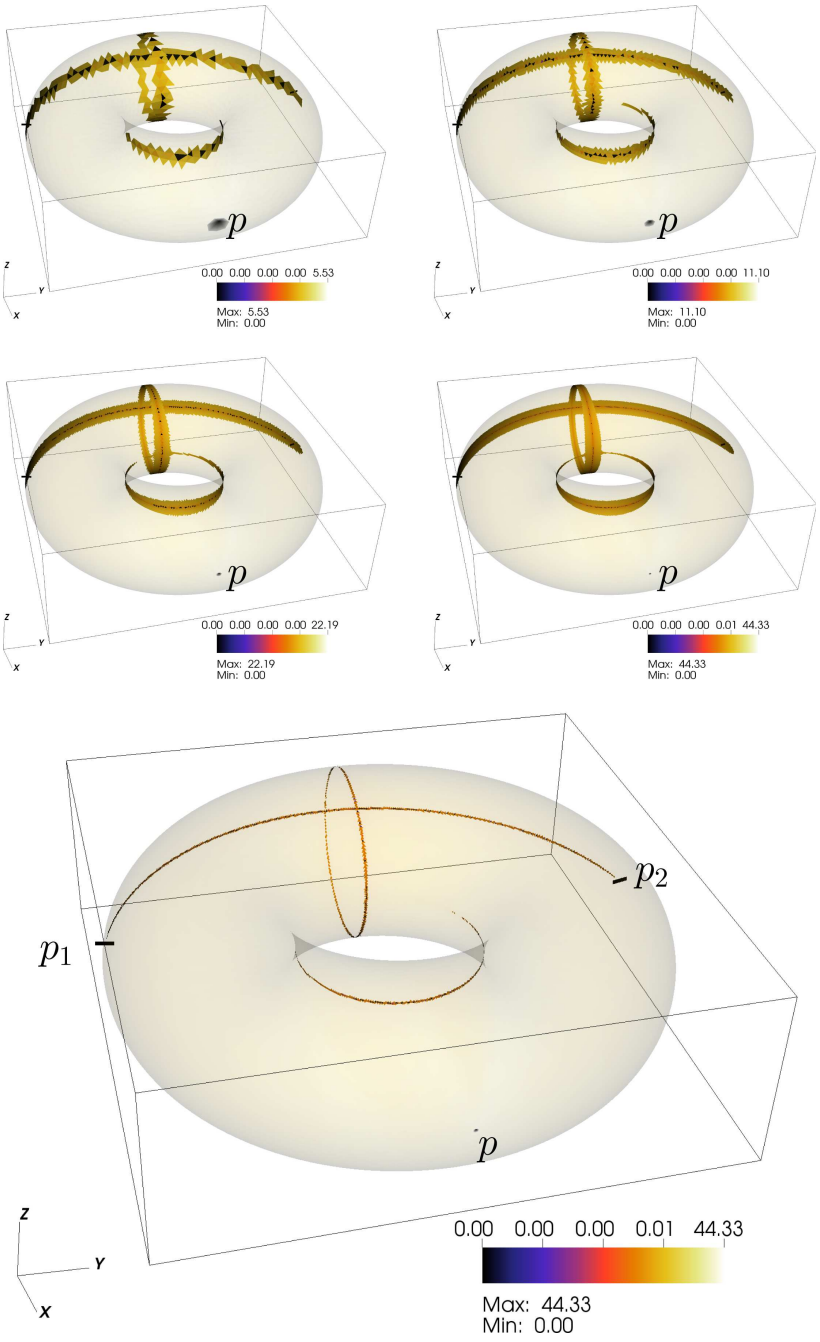

FIGURE 3. Numerical identification of the $C_{p,h,\epsilon}$ of a torus obtained at four uniform mesh refinement levels for $\epsilon = 0.001$. The color map refers to μ_h^* values. The coarsest mesh level contains 2712 nodes and 5424 triangles. The two segments in black intersect the surface of the torus at points p_1 and p_2 described in Figure 1. The bottom panel shows the $C_{p,h,\epsilon}$ for $\epsilon = 0.0001$ on the finest grid level.

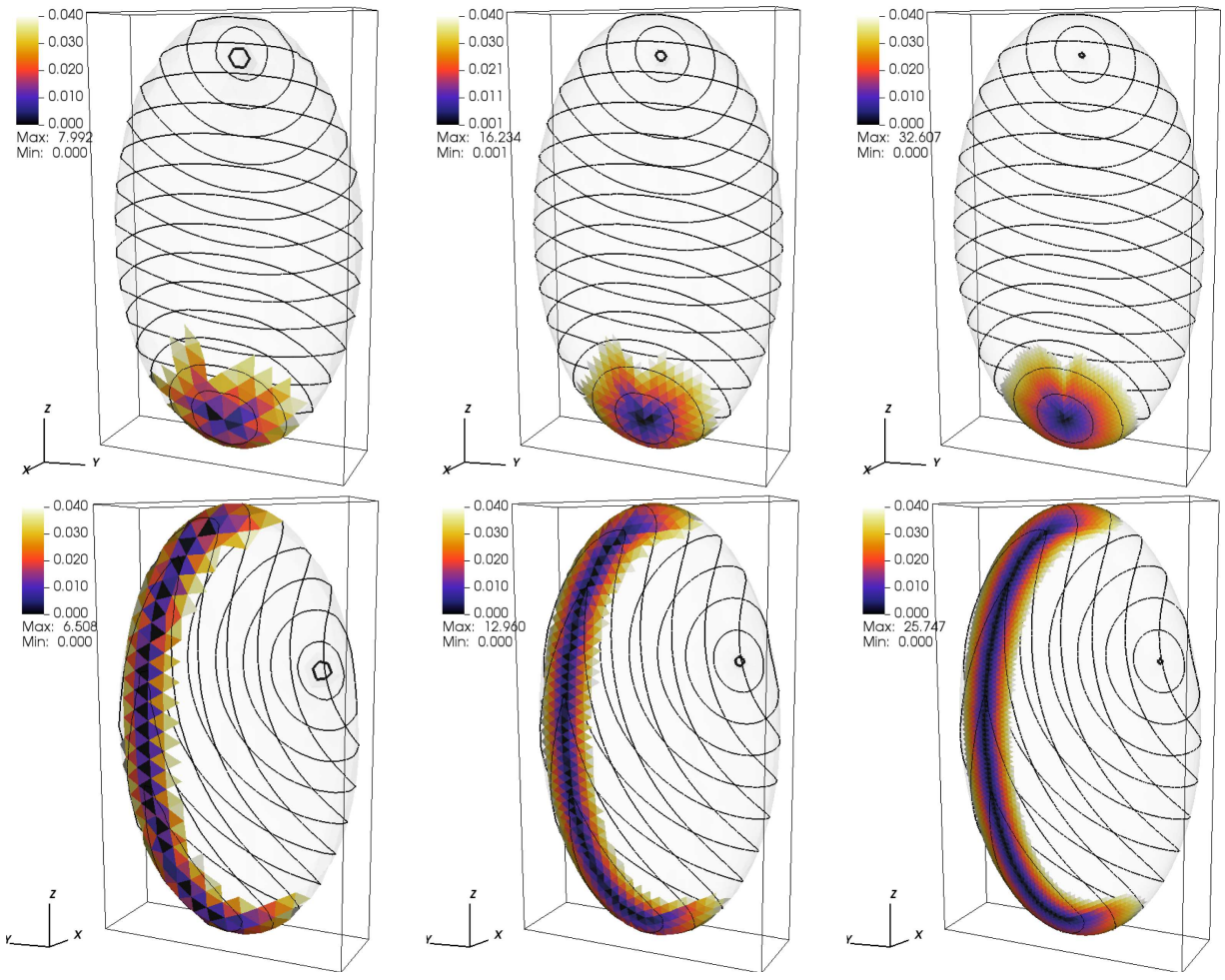

FIGURE 4. Ellipsoid $(x/0.2)^2 + (y/0.6)^2 + (z)^2 = 1$. *Upper panels*: spatial distribution of μ_h^* for the point $p^1 = (-0.115470, 0, 0.816497)$. We report the results for three meshes, one the conformal refinement of the other, with the first having 534 nodes and 1064 triangles, and the latter 8514 nodes 17 024 triangles. The point p^1 is located "behind" the visible ellipsoid and it is marked with a black circle. We report only those triangles where μ_h^* is below 0.04. We also report the contour lines of u_h^*. *Lower panels*: same plots for the point $p^2 = (-0.151128, -0.350718, 0.295520)$.

The final test-case, again taken from [30], looks for the cut locus of the quartic equation surface defined by

$$Q := \left\{(x, y, z) \in \mathbb{R}^3 : x^4 + y^4 + z^4 = 1\right\}$$

with respect to the point $p = (0.533843, 0.800764, 0.844080)$. Figure 5 shows the spatial distribution of μ_h^* obtained on two different triangulations. The first mesh (left panel) is characterized by 34 178 nodes and 68 352 triangles in $\mathcal{T}_h$, where μ_h^* is defined, and 136 712 nodes and 273 408 triangles, in $\mathcal{T}_{h/2}$, where u_h^* lives. The second mesh level (right panel) is exactly four times larger. The approximate zero set of μ_h^* shown on the two refinements in Figure 5 compares well with the approximate cut locus reported in [30].

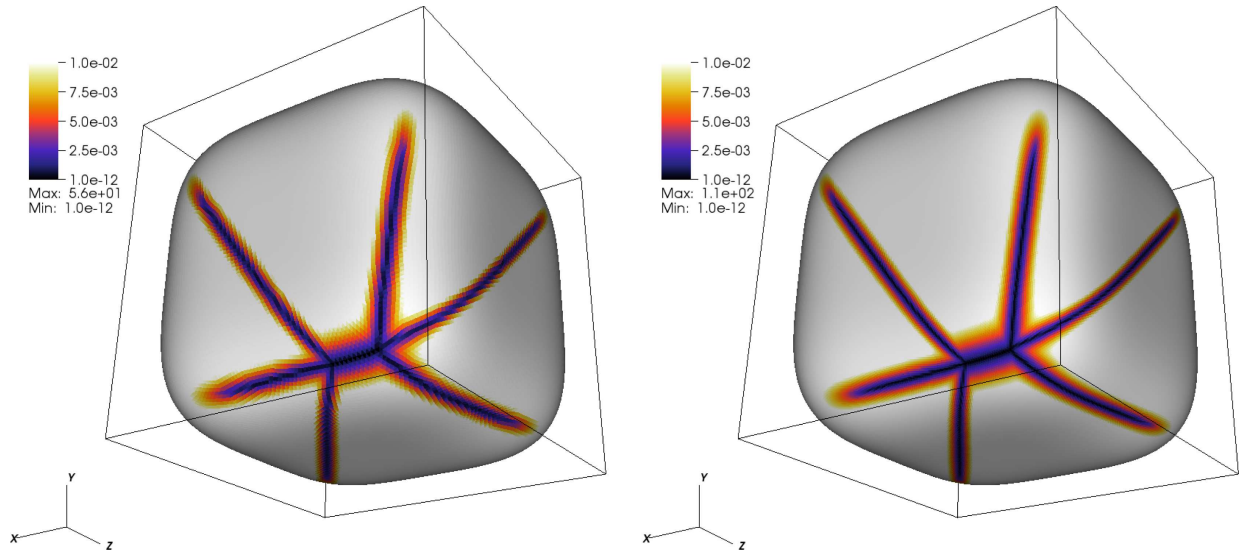

FIGURE 5. Spatial distribution of the μ_h^* on the surface Q using $f^+ = |Q|\delta_p$ with $p = (0.533843, 0.800764, 0.844080)$ and $f = 1$. *Left panel*: result using a mesh containing 34 178 nodes and 68 352 cells. The color scale has its maximum at 0.01 to highlight the region where μ_h^* attains the lowest value. *Right panel*: same results using the conformal refinement of the surface triangulation (136 706 nodes and 273 408 cells).

We would like to note here that our DMK-based approach is much more computationally efficient than [30]. Indeed, the computational cost for these simulations on a laptop computer equipped with a 2014 Intel Core-I5 processor with 8 GB of RAM are 782 and 4606 s for the two meshes. This is to be compared with the computational cost of 35 506 s reported in [30] to solve the same problem on a mesh with 49 152 triangles (with an unspecified CPU). The difference in performance has to be attributed to the fact that the algorithm in [30] has a computational complexity that grows exponentially with the size of the triangulation, while our algorithm is affected by the classical polynomial computational complexity of FEM methods. Finally, we would like to note that the computational cost of our method is comparable if not better to the approach described in [27]. The use of implicit time-stepping in combination with Newton method as proposed in [17], which allows a drastic improvement in computational efficiency, is the next step in our future studies.

6. CONCLUSIONS

We presented a new result showing the one-to-one correspondence between the cut locus of a point p in a Riemannian manifold (M, g) and the zero set of the OTD μ^* solution of the MK equations with $f^+ = \mathrm{d}V_g(M)\delta_p$ and $f^- = \mathrm{d}V_g$. This new PDE-based characterization allows us to exploit standard finite element methods in combination with optimization techniques for the numerical approximation of the cut locus. Based on this result, we proposed a novel numerical approach for the identification of the cut locus of a point on 2d surfaces embedded in $\mathbb{R}^3$ using the DMK method proposed in [4] for the solution of the of the MK equations. Numerical tests on few examples show that the cut locus can be efficiently identified with the developed strategy. The scheme seems to be reliable also for singular sets that have branches, such as those arising in the torus or the quartic surface. Finally, we would like to mention that the proposed DMK-based numerical approach can be easily extended to manifolds with dimension greater than two as long as the numerical solution of the PDE equation (3.1a) is feasible.

Acknowledgements. EF has been supported by the Centro di Ricerca Matematica "Ennio De Giorgi". FF has been partially supported by MIUR-PRIN project 20178CJA2B *New frontiers of Celestial Mechanics: theory and applications.* MP has been partially supported by UniPD-SID-2016 project *Approximation and discretization of PDEs on Manifolds for Environmental Modeling.*

References

[1] P. Albano, On the stability of the cut locus. *Nonlinear Anal. Theory Methods Appl.* **136** (2016) 51–61.
[2] L. Ambrosio, Lecture notes on optimal transport problems. In: *Lecture Notes in Mathematics*. Springer, Berlin, Heidelberg (2003) 1–52.
[3] E. Bachini and M. Putti, Geometrically intrinsic modeling of shallow water flows. *ESAIM: Math. Model. Num. Anal.* **54** (2020) 2125–2157.
[4] L. Berti, E. Facca and M. Putti, Numerical solution of the L^1-optimal transport problem on surfaces. Preprint arXiv:2106.06479 (2021).
[5] L.E. Blumenson, A derivation of n-dimensional spherical coordinates. *Am. Math. Mon.* **67** (1960) 63–66.
[6] B. Bonnard, J.B. Caillau, R. Sinclair and M. Tanaka, Conjugate and cut loci of a two-sphere of revolution with application to optimal control. *Ann. Inst. H. Poincaré Anal. Non Linéaire* **26** (2009) 1081–1098.
[7] B. Bonnard, O. Cots and L. Jassionnesse, Geometric and Numerical Techniques to Compute Conjugate and Cut Loci on Riemannian Surfaces. Springer International Publishing, Cham (2014) 53–72.
[8] G. Bouchitté and G. Buttazzo, Characterization of optimal shapes and masses through Monge–Kantorovich equation. *J. Eur. Math. Soc.* **3** (2001) 139–168.
[9] G. Buttazzo and E. Stepanov, On regularity of transport density in the Monge–Kantorovich problem. *SIAM J. Control Optim.* **42** (2003) 1044–1055.
[10] J.-B. Caillau, O. Cots and P. Martinon, ct: control toolbox – numerical tools and examples in optimal control. Working paper or preprint (Feb. 2022). https://hal.inria.fr/hal-03558975.
[11] I. Chavel, Riemannian Geometry: A Modern Introduction. *Cambridge Studies in Advanced Mathematics*, 2nd edition. Cambridge University Press (2006).
[12] K. Crane, C. Weischedel and M. Wardetzky, Geodesics in heat: a new approach to computing distance based on heat flow. *ACM Trans. Graph.* **32** (2013) 1–11.
[13] L. De Pascale, L.C. Evans and A. Pratelli, Integral estimates for transport densities. *Bull. London Mat. Soc.* **36** (2004) 383–395.
[14] T.K. Dey and K. Li, Cut locus and topology from surface point data. In: *Proceedings of the Twenty-fifth Annual Symposium on Computational Geometry* (2009) 125–134.
[15] G. Dziuk and C.M. Elliott, Finite element methods for surface pdes. *Acta Num.* **22** (2013) 289–396.
[16] L.C. Evans and W. Gangbo, Differential Equations Methods for the Monge–Kantorovich Mass Transfer Problem. Vol. 653. American Mathematical Soc. (1999).
[17] E. Facca and M. Benzi, Fast iterative solution of the optimal transport problem on graphs. *SIAM J. Sci. Comput.* **43** (2021) A2295–A2319.
[18] E. Facca, F. Cardin and M. Putti, Towards a stationary Monge–Kantorovich dynamics: the physarum polycephalum experience. *SIAM J. Appl. Math.* **78** (2018) 651–676.
[19] E. Facca, S. Daneri, F. Cardin and M. Putti, Numerical solution of Monge–Kantorovich equations via a dynamic formulation. *J. Sci. Comput.* **82** (2020) 1–26.
[20] E. Facca, F. Piazzon and M. Putti, L^1 transport energy. *Appl. Math. Optim.* **86** (2022) 1–40.
[21] M. Feldman and R.J. McCann, Monge's transport problem on a riemannian manifold. *Trans. Amer. Math. Soc.* **354** (2001) 1667–1697.
[22] M. Feldman and R.J. McCann, Uniqueness and transport density in monge's mass transportation problem. *Calc. Var. Part. Diff. Equ.* **15** (2002) 81–113.
[23] A. Figalli and L. Rifford, Mass transportation on sub-riemannian manifolds. *Geom. Funct. Anal.* **20** (2010) 124–159.
[24] A. Figalli and C. Villani, An approximation lemma about the cut locus, with applications in optimal transport theory. *Methods App. Anal.* **15** (2008) 149–154.
[25] A. Figalli, L. Rifford and C. Villani, Tangent cut loci on surfaces. *Differ. Geom. Appl.* **29** (2011) 154–159.
[26] F. Générau, E. Oudet and B. Velichkov, Cut locus on compact manifolds and uniform semiconcavity estimates for a variational inequality. Preprint arXiv:2006.07222 (2020).
[27] F. Générau, E. Oudet and B. Velichkov, Numerical computation of the cut locus via a variational approximation of the distance function. *ESAIM: Math. Model. Num. Anal.* **56** (2022) 105–120.
[28] J. Gravesen, S. Markvorsen, R. Sinclair and M. Tanaka, The cut locus of a torus of revolution. *Asian J. Math.* **9** (2005) 103–120.
[29] J.I. Itoh and K. Kiyohara, The cut loci and the conjugate loci on ellipsoids. *Manuscr. Math.* **114** (2004) 247–264.
[30] J.I. Itoh and R. Sinclair, Thaw: a tool for approximating cut loci on a triangulation of a surface. *Exp. Math.* **13** (2004) 309–325.
[31] J.I. Itoh and M. Tanaka, The Lipschitz continuity of the distance function to the cut locus. *Trans. Amer. Math. Soc.* **353** (2001) 21–40.

[32] J. Jost, Riemannian Geometry and Geometric Analysis. Vol. 42005. Springer (2008).
[33] B.F. Kimball, Geodesics on a toroid. *Am. J. Math.* **52** (1930) 29–52.
[34] C. Mancinelli, M. Livesu and E. Puppo, Practical computation of the cut locus on discrete surfaces. *Comput. Graph Forum* **40** (2021) 261–273.
[35] C. Mantegazza and A.C. Mennucci, Hamilton-Jacobi equations and distance functions on Riemannian manifolds. *Appl. Math. Optim.* **47** (2003) 1–25.
[36] M.K. Misztal, J.A. Bærentzen, F. Anton and S. Markvorsen, Cut locus construction using deformable simplicial complexes. In: 2011 Eighth International Symposium on Voronoi Diagrams in Science and Engineering (ISVD). IEEE (2011) 134–141.
[37] J.-M. Morvan, Generalized Curvatures. Vol. 2 of *Geometry and Computing*. Springer Science & Business Media, Berlin, Heidelberg (2008).
[38] P.-O. Persson and G. Strang, A simple mesh generator in Matlab. *SIAM Rev.* **46** (2004) 329–345.
[39] A. Pratelli, Equivalence between some definitions for the optimal mass transport problem and for the transport density on manifolds. *Ann. Mat. Pura App.* **184** (2005) 215–238.
[40] T. Sakai, Riemannian Geometry. Vol. 149, American Mathematical Society (1996).
[41] F. Santambrogio, Absolute continuity and summability of transport densities: simpler proofs and new estimates. *Calc. Var. Part. Diff. Equ.* **36** (2009) 343–354.
[42] F. Santambrogio, Optimal Transport for Applied Mathematicians. Birkäuser, NY (2015).
[43] R. Sinclair and M. Tanaka, Loki: software for computing cut loci. *Exp. Math.* **11** (2002) 1–25.
[44] A.-K. Tornberg and B. Engquist, Regularization techniques for numerical approximation of PDEs with singularities. *J. Scient. Comput.* **19** (2003) 527–552.
[45] A.-K. Tornberg and B. Engquist, Numerical approximations of singular source terms in differential equations. *J. Comp. Phys.* **200** (2004) 462–488.
[46] C. Villani, Topics in Optimal Transportation. Vol. 58 of *Graduate Studies in Mathematics*. American Mathematical Society (2003).
[47] C. Villani, Optimal Transport: Old and New. Vol. 338. Springer Science & Business Media (2008).
[48] C. Villani, Regularity of optimal transport and cut locus: from nonsmooth analysis to geometry to smooth analysis. *Discrete Contin. Dyn. Syst. Ser. A* **30** (2011) 559–571.